



HAL
open science

Dual-Wideband Dual-Circularly-Polarized Shared-Aperture Reflectarrays with a Single Functional Substrate for K-/Ka-Band Applications

X. Tong, Z Jiang, Y. Li, F. Wu, R Sauleau, W. Hong

► **To cite this version:**

X. Tong, Z Jiang, Y. Li, F. Wu, R Sauleau, et al.. Dual-Wideband Dual-Circularly-Polarized Shared-Aperture Reflectarrays with a Single Functional Substrate for K-/Ka-Band Applications. *IEEE Transactions on Antennas and Propagation*, 2022, 70 (7), pp.5404-5417. 10.1109/TAP.2022.3145484 . hal-03719694

HAL Id: hal-03719694

<https://hal.science/hal-03719694>

Submitted on 19 Jul 2022

HAL is a multi-disciplinary open access archive for the deposit and dissemination of scientific research documents, whether they are published or not. The documents may come from teaching and research institutions in France or abroad, or from public or private research centers.

L'archive ouverte pluridisciplinaire **HAL**, est destinée au dépôt et à la diffusion de documents scientifiques de niveau recherche, publiés ou non, émanant des établissements d'enseignement et de recherche français ou étrangers, des laboratoires publics ou privés.

Dual-Wideband Dual-Circularly-Polarized Shared-Aperture Reflectarrays with a Single Functional Substrate for K -/ Ka -Band Applications

Xuanfeng Tong, *Student Member, IEEE*, Zhi Hao Jiang, *Member, IEEE*, Yuan Li, *Student Member, IEEE*, Fan Wu, *Member, IEEE*, Ronan Sauleau, *Fellow, IEEE*, and Wei Hong, *Fellow, IEEE*

Abstract—We report here the design and experiments of dual-wideband dual-circularly-polarized (dual-CP) shared-aperture reflectarrays (RAs) operating at K -/ Ka -band utilizing a single functional substrate. By coupling the adjacent but separated resonances of H-shaped aperture and circular patch and utilizing the shorted microstrip phase delay lines, the proposed RA cells can offer wideband performance. Then, these RA cells are interleaved in a shared aperture for dual-band operation. By combining the dynamic phase and Berry phase compensation techniques, the RA cells can independently control the reflective phase delay of orthogonal CP beams at both of the targeted bands, providing four degrees of freedom for beamforming. The diffractive property of an infinite periodic gradient array of the interleaved K - and Ka -band cells is investigated, which verifies the wideband performance of the proposed cells. Two RAs with a thin panel thickness of $0.27 \lambda_K$ (λ_K is the free-space wavelength at K -band) are fabricated and characterized, generating symmetrically- and asymmetrically-distributed dual-wideband dual-CP beams at K -/ Ka -band, respectively. The measured bandwidths for the two RAs are wider than 14.1% for K -band right-/left-handed CP beams and about 11% for Ka -band right-/left-handed CP beams with both the gain variation and axial ratio smaller than 2 dB.

Index Terms—Dual-band, dual-circularly-polarization, millimeter-wave, reflectarrays, shared-aperture.

I. INTRODUCTION

HIGH-gain circularly-polarized (CP) antennas are amenable for long-distance wireless communications [1], such as

Manuscript received Aug. 23, 2021. This work was supported in part by National Natural Science Foundation of China (NSFC) under Grants 62122019, 61801109 and 61901106, in part by the Fundamental Research Funds for the Central Universities under Grant 2242021k30041, in part by the Research Institute of China Mobile, and in part by the High Level Innovation and Entrepreneurial Research Team Program in Jiangsu. (*Corresponding author: Zhi Hao Jiang.*)

X. F. Tong and Y. Li are with the State Key Laboratory of Millimeter Waves, School of Information Science and Engineering, Southeast University, Nanjing 210096, China.

Z. H. Jiang, F. Wu, and W. Hong are with the State Key Laboratory of Millimeter Waves, School of Information Science and Engineering, Southeast University, Nanjing 210096, China (e-mail: zhihao.jiang@seu.edu.cn).

R. Sauleau is with Univ Rennes, ICNRS, IETR - UMR 6164, F-35000 Rennes, France.

point-to-point communications, satellite communications (SatCom), and so on. Phased-arrays [2] and parabolic reflectors [3] are conventional antenna solutions for generating high-gain beams. However, the phased-arrays suffer from high cost and high-level power consumption, while the curved structures of parabolic reflectors restrict their applications in integrated systems. Therefore, the reflectarray (RA) was proposed as an alternative promising solution since it can eliminate the shortcomings and combine the advantages of phased-arrays and reflector antennas [4]. With the assistance of space-fed configurations and sub-wavelength multi-functional phase-shifting cells, RAs can achieve wideband [5]-[8], multi-band [9]-[10], multi-polarizations [11]-[12], and beam scanning [13]-[15] capabilities for controllable beamforming and/or increasing the spectrum efficiency.

Recently, dual-band RAs have been widely investigated due to their potential for multi-functional operation with a single aperture, which can be achieved by employing phase synthesis technique [16], [17], dual-band shared-aperture elements [18]-[20], concentric dual-band rotational elements [21]-[23], and dual functional substrates with each substrate working at a single band [24]-[25]. Dual-band RAs with different frequency ratios ranging from 1.5 to 2.5 have been reported by using wideband phoenix elements that can provide a full 360° phase coverage at both bands [17]. The restriction of this work is that the beam directions at the two bands were kept the same. Shared-aperture methods have also been applied in dual-band RA designs. A dual-band shared-aperture RA with a frequency ratio of 1.6 is presented using the parallel dipoles elements [19], achieving a 2-dB gain bandwidth of 20% in the lower band and 5% in the upper band. Dual-band RAs operating at 20 and 30 GHz are reported in [21] and [22] by employing concentric dual-band elements, both with a 1-dB gain bandwidths of less than 5.5% and 7% in the lower and upper band, respectively. Besides the realization of dual-band performance using a single functional substrate [17]-[23], dual-functional-substrate RAs have also been exploited to achieve dual-band features with the advantages of simplifying the design and arrangement of RA elements, as well as enabling almost independent element spacing at both bands. In [24], split-rings elements are used for both the X - and Ka -bands, where the X -band RA layer is

installed above the Ka -band one. It is noteworthy that the upper-layer structure should behave as transparent in the operational band of the lower-layer RA. Moreover, in the multi-functional-substrate dual-band RA designs, a frequency selective surface (FSS) can be employed to reduce the coupling between the RA elements working at different operation bands [20], [23], [25].

Apart from dual-band RAs, dual-CP RAs with independent control of orthogonal CP beams have recently gained much attention due to their frequency-reuse capability particularly for SatCom applications. Basically, three methods have been reported for achieving true dual-CP RA at the same frequency band [26]. The first approach separates the left-handed CP (LHCP) and right-handed CP (RHCP) waves and compensates their phases at different functional substrates [27]-[28]. As presented in [28], the upper-layer works not only as the phase-shifting surface for LHCP waves, but also as a circularly polarization selective surface (CPSS) which reflects LHCP and transmits RHCP waves. It achieves a fractional bandwidth of 9.4% for axial ratio (AR) < 3.5 dB with a gain variation of less than 1.5 dB and a panel thickness of $1.8\lambda_c$, where λ_c is the free-space wavelength at the center frequency. For the second method, two functional substrates are also employed. The upper-layer is a linear-to-circular polarizer, while the lower-layer works as a dual-linearly-polarized (dual-LP) RA [29]-[30], possessing a total panel thickness on the order of $0.9\lambda_c$ or even a few wavelengths. The drawback of this method is that it introduces higher insertion loss since the waves go through the linear-to-circular polarizer twice. The third approach utilizes only a single functional substrate, which can dramatically reduce the RA complexity. By simultaneously applying Berry phase (BP), i.e., variable self-rotation induced phase delay, and dynamic phase (DP), i.e., variable delay lines or variable sizes induced phase delay, RHCP and LHCP waves can be independently manipulated [26], [31]-[33]. Metal-backed dual-LP aperture coupled patch element with variable-length delay lines has been employed to achieve dual-CP RAs, exhibiting a bandwidth of 14.7% with AR < 2 dB and gain variation < 1 dB [31]. Recently, broadband dual-CP RAs using anisotropic impedance surface enabled elements [26] have been presented, yielding a bandwidth of 30% with AR < 0.5 dB and gain variation < 1 dB.

RAs with dual-band dual-CP features are highly-desirable for applications such as high throughput satellite (HTS) communications due to their simultaneous polarization and frequency discrimination capability. So far, only a few RA designs have been reported for accomplishing the dual-band dual-CP performance in the literature [34]-[35], [37]. A dual-band dual-CP RA with a frequency ratio of 1.16 is presented in [34]. Two equilateral triangular patches - each cascaded with a hybrid coupler - were employed to operate at 8.6 and 10 GHz, respectively, thereby forming a dual-band interleaved RA. Four open-ended variable delay lines terminating the two hybrid couplers were used to independently compensate the required phase for RHCP and LHCP at both frequencies. However, the narrow gain bandwidths and large element separation of 22.5 mm, i.e., $0.64\lambda_L$ and $0.75\lambda_H$, where λ_L and λ_H are the free-space wavelength at low and high bands would restrict its potential

applications. Alternatively, dual-band dual-CP RA can be implemented by replacing the single-band CP-to-LP polarizer and the underneath dual-LP RA into dual-band ones. In [35], a dual-band CP-to-LP polarizer and a dual-band dual-LP element are integrated to act as a dual-band dual-CP RA operating at K - and Ka -bands with a total panel thickness of $1.23\lambda_L$. However, due to the bandwidth limitation of both the CP-to-LP polarizer [36] and the dual-band dual-LP element, the 1-dB gain bandwidths are only 1.65% and 2.56% in the lower and upper band, respectively. More recently, another dual-band dual-CP RA with a frequency ratio of 2.4 was reported by utilizing multi-functional-substrate RA elements separated by an FSS [37]. It obtains bandwidths of 14.4% (11.7%) and 7.1% (11.8%) for the RHCP and LHCP beams at Ku -band (Ka -band) with both the gain variation and AR < 3 dB. It has a panel thickness of $0.52\lambda_L$ and achieves aperture efficiencies of 14.5% and 15.6% at the two bands.

In this paper, the design and experiments of dual-wideband dual-CP K -/ Ka -band RAs using only a single functional substrate are reported for the first time, as opposite to Ref. [35] where two substrates were employed (one for dual-band CP-to-LP polarizer, and one for dual-band dual-LP RA), or even to Ref. [37] where three functional substrates were used (one for Ku -band RA, one for Ka -band RA, and one for the FSS in the middle). Miniaturized K -band cells together with Ka -band cells are interleaved in the same aperture for dual-band operation, while BP and DP are simultaneously utilized to acquire the independent dual-CP beamforming at both bands. Two RAs with four beams pointing at prescribed directions are designed, fabricated, and characterized. The article is organized as follows. Section II introduces the configuration of the RA, the scattering properties of the dual-wideband shared-aperture cells, and 3×3 bit dual-CP phase compensation strategies. Decoupling between the K - and Ka -band cells, as well as the oblique incidence performance of the RA cells are also provided. Section III presents the diffraction analysis and wave-bending behavior of a linearly gradient array composed of the designed RA cells. In Section IV, the design and experimental results of two RAs are reported, one with dual-CP beams symmetrically distributed in the y - z plane and the other one has dual-CP beams asymmetrically distributed in the x - z and y - z planes. Finally, conclusions are drawn in Section V.

II. RA CONFIGURATION AND DUAL-WIDEBAND DUAL-CP SHARED-APERTURE PHASE-COMPENSATING CELL DESIGNS

A. RA Configuration

The configuration of the dual-wideband dual-CP shared-aperture RA is presented in Fig. 1; it is illuminated by K - and Ka -band dual-CP feed horns. Both K - and Ka -band horns are vertically placed above the RA with different focal distances of F_K and F_{Ka} . It can generate four pencil beams which are K -/ Ka -band RHCP beam pointing at $(\theta_R, \varphi_R)_{K/Ka}$ under K -/ Ka -band RHCP horn illumination and K -/ Ka -band LHCP beam directing at $(\theta_L, \varphi_L)_{K/Ka}$ due to K -/ Ka -band LHCP horn illumination, respectively. The four generated beams can be independently pointed to arbitrary directions within a certain field-of-view,

which is constrained primarily by the angular response of the RA cells, by simultaneously exploiting wideband cells, shared-aperture method, as well as joint BP and DP phase compensation techniques.

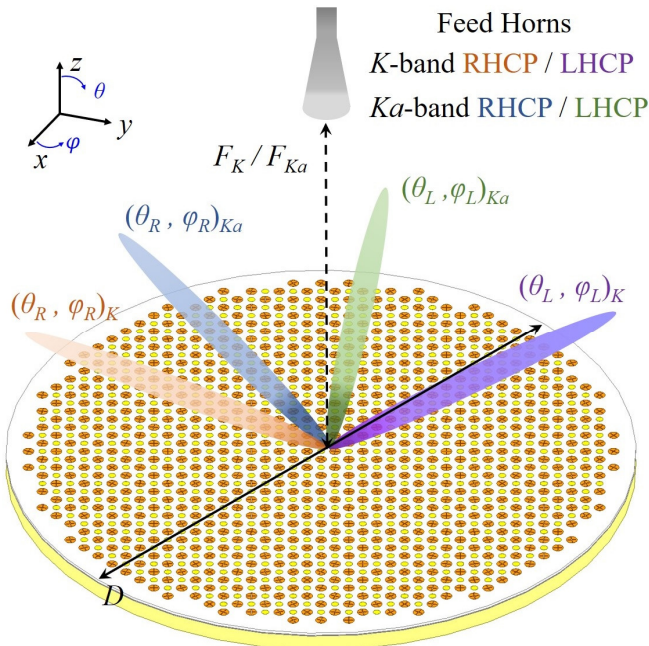


Fig. 1. Configuration of the dual-wideband dual-CP RA. The four generated beams can point to arbitrary directions of $(\theta_{R/L}, \varphi_{R/L})_{K/Ka}$ within a certain field-of-view, where the subscripts R/L represents RHCP/LHCP waves, and K/Ka indicates K -/ Ka -band.

B. Dual-Wideband Shared-Aperture Element Design

For RAs with a good performance, each RA cell should be able to efficiently receive the wave emitted from the feed and reradiate with an appropriate phase delay, thereby constructing the desirable wavefront. Accordingly, for RAs cells with cascaded antenna-phase shifter structures, the infinite antenna array simulation method can be utilized to evaluate the performance of the RA cells [see Fig. 2(a)]. The configuration of the dual-wideband shared-aperture element is shown in Fig. 2. It has two Rogers 4003 substrates with a relative permittivity of 3.55 and a loss tangent of 0.0027, which are bonded together using Rogers 4450F with a relative permittivity of 3.52 and a loss tangent of 0.004 [see Fig. 2(a)]. Two Rogers 4003 substrates have thicknesses of 0.813 mm and 0.203 mm from top to bottom, while the thickness is 0.1 mm for the bonding film. For both K - and Ka -band elements, the circular patch is etched on the top surface of the top substrate, meanwhile, the ground plane with two H-shaped slots and two microstrip feedlines are placed on the top and bottom surfaces of the bottom substrate, respectively. A pair of orthogonal H-shaped slots and two microstrip feedlines are used for dual-LP response. In addition, two crossed slots are introduced at the center of K -band patch for size reduction. A metal reflector plane is located underneath the microstrip feedlines at a distance of 3 mm, yielding the total element thickness of 4.1 mm, i.e., $0.27\lambda_K$, where λ_K is the free-space wavelength at 20 GHz. The K - and Ka -band elements can be interleaved in the same aperture for dual-band operation [see Fig. 1]. The dual-wideband shared-

aperture element occupies a footprint of $6 \text{ mm} \times 6 \text{ mm}$, which indicates the element spacing is $0.4\lambda_K$ at K -band and $0.6\lambda_{Ka}$ at Ka -band, where λ_{Ka} is the free-space wavelength at 30 GHz.

In order to verify the capability of efficient wave reception and radiation of the elements, a simulation setup using high-frequency structure simulator (HFSS) software is adopted, as shown in Fig. 2(a). Master and slave periodic boundaries are used to emulate the infinite array environment. It should be noted that Port 1, Port 3, and mode1 of the Floquet port correspond to the x -polarization, while Port 2, Port 4, and mode2 of the Floquet port excite the y -polarization. With this setup, the simulated S -parameters can be obtained to assess the performance of the proposed dual-wideband shared-aperture elements, where S_{nn} ($n = 1, 2, 3, 4$) represents the reflection coefficient of each port, $S_{m\text{moden}}$ ($n = 1, 2, m = 1, 2, 3, 4$) indicates the ability to receive/radiate waves with the same or different polarization.

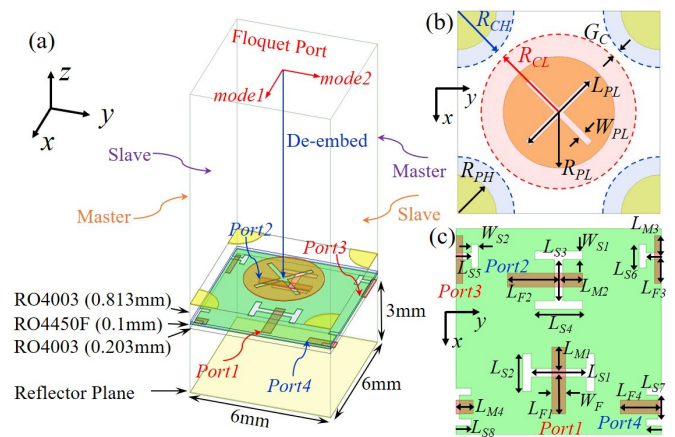


Fig. 2. (a) 3-D view of the dual-wideband shared-aperture RA element together with simulation setup in HFSS. (b) Geometry of the K - and Ka -band patches, where the highlighted areas encompassed by red/blue dashed lines are the restricted rotating areas for K -/ Ka -band elements. (c) Geometries of the ground plane and microstrip feedlines at K -/ Ka -band. The K -band element geometrical dimensions are $R_{CL} = 2.4$, $G_C = 0.14$, $R_{PL} = 1.65$, $L_{PL} = 2.6$, $W_{PL} = 0.2$, $W_{S1} = 0.25$, $L_{S1} = 1.5$, $L_{S2} = 1.1$, $L_{S3} = 0.95$, $L_{S4} = 1.5$, $L_{M1} = 0.7$, $L_{M2} = 0.7$, $W_F = 0.4$, $L_{F1} = 1$, $L_{F2} = 1$, while the Ka -band element geometrical dimensions are $R_{CH} = 1.7$, $R_{PH} = 1.15$, $W_{S2} = 0.2$, $L_{S5} = 0.9$, $L_{S6} = 0.7$, $L_{S7} = 0.7$, $L_{S8} = 0.9$, $L_{M3} = 0.5$, $L_{M4} = 0.6$, $L_{F3} = 0.8$, $L_{F4} = 0.8$, all in millimeters.

First, the antenna elements operating at K - and Ka -bands that make up the dual-wideband dual-CP RA are studied separately. Dual-LP aperture-coupled circular patch antennas are utilized for both K - and Ka -band elements, where the two orthogonal H-shaped slots cut on the ground plane are used for wave coupling from the microstrip feedlines to patches [see Fig. 2]. By combining the separated but adjacent resonances of the circular patch and H-shaped slot, manifested by the two deeps of S_{nn} in Fig. 3(a), the proposed antenna elements exhibit a wide impedance bandwidth [38]. The insets of Fig. 3(a) show the vectorial surface currents distributed on the patch and ground plane corresponding to the two resonances (x -polarization at 20 GHz and y -polarization at 30 GHz are taken as examples). Moreover, a metal reflector plane is introduced underneath the element to suppress the back radiation of the slot [39]. Eventually, as demonstrated by Fig. 3(a), both the proposed K - and Ka -band antenna elements achieve an $S_{11} < -13$ dB

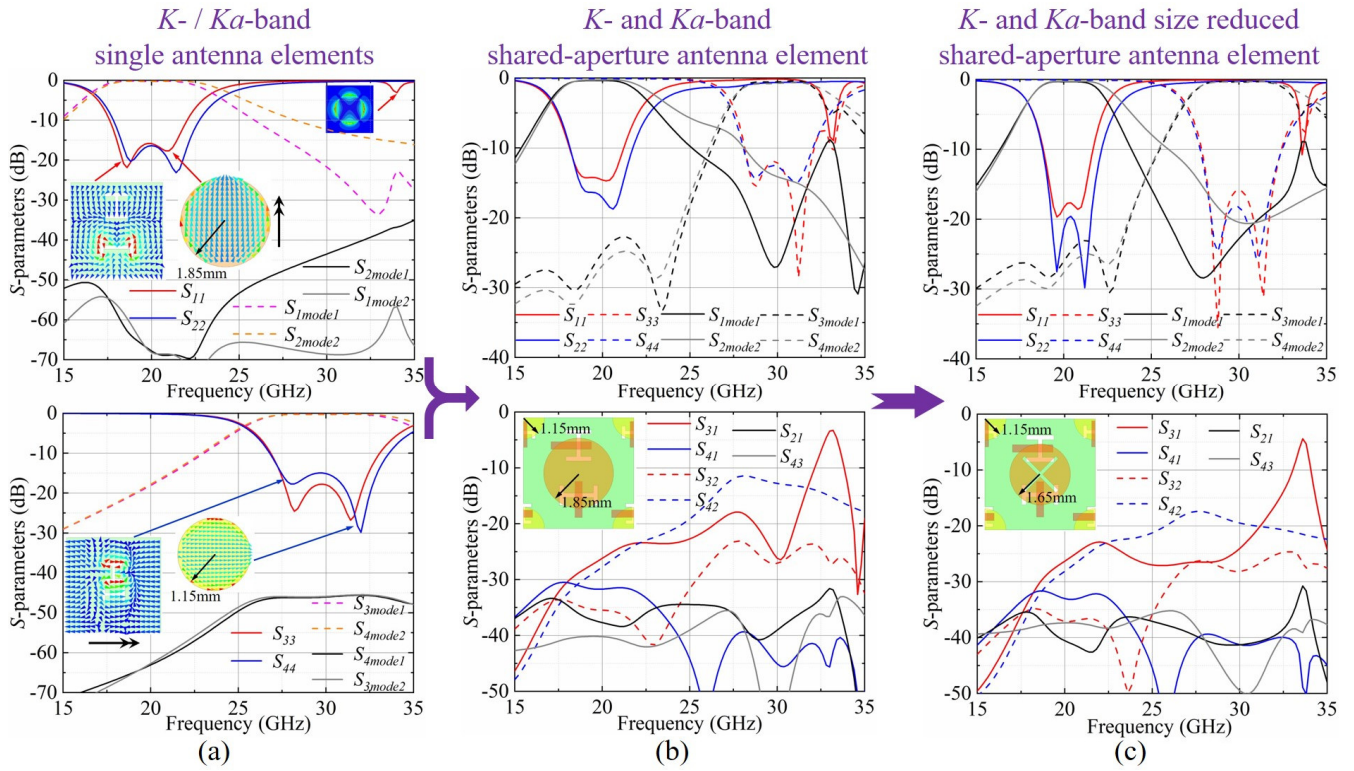


Fig. 3. (a) Simulated S -parameters of the separated K -/ Ka -band antenna elements at normal incidence, (b) simulated S -parameters of the dual-wideband shared-aperture antenna element at normal incidence without size reduction, (c) simulated S -parameters of the proposed dual-wideband shared-aperture antenna element at normal incidence.

TABLE I DIMENSIONS OF SHORT-ENDED DELAY LINES AND H-SHAPED SLOTS OF EIGHT PROPOSED CELLS AT K - AND Ka -BANDS (UNIT: MM).

Cell _{L/H} number	K -band								Ka -band							
	1	2	3	4	5	6	7	8	1	2	3	4	5	6	7	8
L_{S1}	1.6	1.6	1.6	1.6	1.6	1.55	1.5	1.6	1	1	0.95	0.9	0.85	0.8	0.75	0.7
L_{S2}	1	1	1	1	1	1	1	1	0.7	0.7	0.7	0.7	0.7	0.7	0.7	0.7
L_{F1}	3.5	3.93	4.09	4.27	4.77	5.19	5.5	5.73	2.24	2.45	3.05	3.52	3.78	3.94	4.1	4.26
L_{S3}	0.95	0.95	0.95	0.95	0.95	0.95	0.95	0.95	0.6	0.7	0.7	0.8	0.9	0.9	0.9	0.9
L_{S4}	1.4	1.4	1.4	1.4	1.4	1.4	1.4	1.4	1.08	1	0.9	0.8	0.7	0.7	0.7	0.7
L_{F2}	1.13	1.5	1.97	2.38	2.79	3.18	3.68	3.86	1.15	1.27	1.64	1.76	1.93	2.22	2.53	2.82

bandwidth of around 18.5% for both linear polarizations, within which the receiving/radiating insertion loss is smaller than 0.5 dB. Importantly, the cross-polarization level of the element is below -45 dB, indicating a high isolation between the orthogonal LP ports [see Fig. 3(a)].

Second, in order to realize dual-band performance using a single functional substrate, K - and Ka -band elements are interleaved to share the same aperture of the RA. When they are interlaced directly as presented in Fig. 3(b), the -10 dB impedance bandwidths get slightly narrowed, but are still wider than 15.8% and 13% at K - and Ka -bands, respectively. However, due to the high-order TM_{21} mode of the K -band patch resonating at 33.2 GHz [see inset in Fig. 3(a)], which is closed to the Ka -band, the mutual couplings (S_{31} and S_{42}) in the same polarization reaches about -12 dB. In order to reduce such coupling, two crossed slots are etched out on the K -band patch [see Fig. 3(c)], resulting in a radius reduction from 1.85 mm to 1.65 mm. As a consequence, the mutual couplings of S_{31} and S_{42} are reduced.

As a summary, the dual-wideband shared-aperture element in Fig. 3(c) achieves a joint $S_{11} < -13$ dB and 0.5-dB insertion

loss bandwidth of 11.4% (19.1 – 21.4 GHz) and 12% (28.3 – 31.9 GHz) at K - and Ka -bands, respectively. Within these bands, the levels of all mutual coupling coefficients remain smaller than -17 dB.

C. RA Unit Cells for 3×3 Bit Dual-CP Phase Compensation

The K - and Ka -band shared-aperture elements can be further modified to form RA cells by replacing the orthogonal microstrip feedlines with short-ended microstrip delay lines. It can be observed from our previous work that, in order to manipulate independently the phase delays of orthogonally CP waves, the K - and Ka -band cells should possess (1) 180° LP reflection phase difference along the two optical axes, (2) proper in-plane rotation angles determined by the desirable phase difference between the RHCP and LHCP waves, and (3) a minimum reflection phase coverage of 180° [26]. To meet the first requirement, the length difference between the two microstrip delay lines is set to be $\lambda_{gK}/4$ and $\lambda_{gKa}/4$ for K - and Ka -band cells, where λ_{gK} and λ_{gKa} are the guided wavelength at K - and Ka -bands, respectively. For the second demand, the K - and Ka -band cells should be able to rotate freely around the patch

center without causing mutual interaction [see Fig. 2(b)]. In order to fulfill the third condition, microstrip delay lines with a variable length are employed to achieve the 180° DP coverage at both bands. It should be noted that by introducing a cell rotation of 90° to all the cells, a full 360° coverage can be achieved.

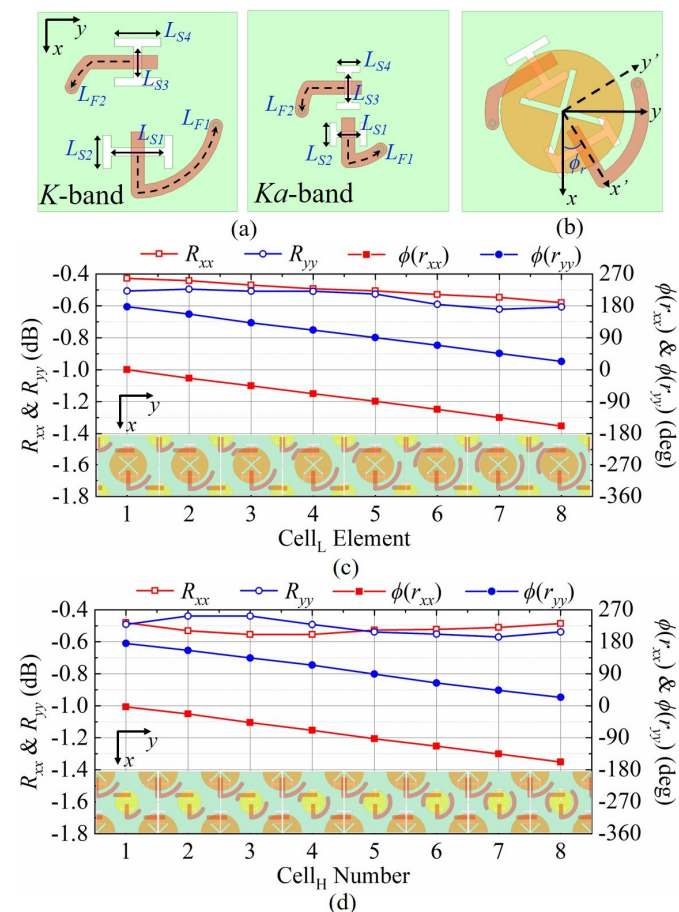


Fig. 4. (a) Geometries of K - and Ka -band RA cells with only their ground plane and phase delay lines shown. (b) The illustration of in-plane rotation angle ϕ_r (K -band cell is taken as an example). Simulated reflection magnitudes and phases at normal incidence for the 8 cells at (c) 20 GHz and (d) 30 GHz.

In this design, for the purpose of realizing 3×3 bit dual-CP phase compensation, 4 bit LP cells with a reflective half-waveplate response and a phase gradient of 22.5° need to be designed, resulting in 8 required cell designs. In order to obtain the linear phase change in a wide bandwidth, the dimensions of the short-ended delay lines and H-shaped slot are optimized simultaneously [6]. Alternatively, open-ended microstrip delay lines can also be used for reducing the manufacturing complexity. However, the open-ended microstrip delay lines may cause resonance due to their floating structures, resulting in increased insertion loss. In contrast, the short-ended microstrip delay lines can shift this resonance to frequencies outside the operational band, thereby improving the linearity of the reflective phase compensation in a wide bandwidth. The geometries and dimensions of the 8 proposed cells at K - and Ka -bands are provided in Fig. 4(a) and Table I. The simulated reflection magnitudes and phases at 20 and 30 GHz are shown in Figs. 4(c) and (d), with an averaged reflection magnitude of around -0.5 dB. It can be seen that (1) each cell owns a 180° LP

reflection phase difference along the two optical axes, i.e., $\phi(r_{xx}) = \phi(r_{yy}) - 180^\circ$, and (2) the 8 cells realize a 180° reflection phase coverage such that a full 360° reflection phase coverage can be achieved by applying a 90° rotation to all of them. In addition, the simulated reflection magnitudes and phases of the proposed K - and Ka -band cells are presented in Fig. 5 as a function of frequency. The reflection magnitudes are all above -1 dB in the frequency ranges of 19.1 – 21.7 GHz and 29.1 – 32.6 GHz, while the reflection phases exhibit a quasi-linear lineshape in these bands.

All the designed cells can reflect CP waves without handedness flip, due to the fact that the reflection phases along the two optical axes of these cells have a 180° difference, as shown in Figs. 4(c) and (d) [40]. The LP scattering parameters can be transformed into CP scattering parameters for evaluating the CP reflection performance of the RA cells [31]. The co-polarized CP (R_{RR} , R_{LL}) and cross-polarized CP (R_{RL} , R_{LR}) reflection magnitudes, along with co-polarized CP reflection phases ($\phi(r_{RR})$, $\phi(r_{LL})$) are provided in Fig. 6. In the frequency ranges of 19.5 – 21.1 GHz and 29.2 – 31.2 GHz, R_{RR} and R_{LL} are all above -0.8 dB, while R_{RL} and R_{LR} are below -15 dB [see Fig. 6]. Meanwhile, the CP reflection phases, i.e., $\phi(r_{RR})$ and $\phi(r_{LL})$ have a progressive phase difference of 22.5° .

When additional in-plane rotation ϕ_r determined by the difference between $\phi(r_{RR})$ and $\phi(r_{LL})$ [see Fig. 4 (b)] is applied to the 8 designed RA cells according to Table II, a library of 64 cells at K -band and 64 cells at Ka -band can be obtained providing the desirable 3×3 bit dual-CP phase delay at both bands. The resulting co-polarized CP reflection phases at 20 GHz and 30 GHz are shown in Figs. 7(a) and (b), where a phase gradient of 45° (3 bit) is achieved for both the RHCP and LHCP waves independently. In addition, the corresponding co-polarized CP reflection magnitudes are all above -0.8 dB (not shown here) since they are almost not affected by the in-plane rotation of the RA cells.

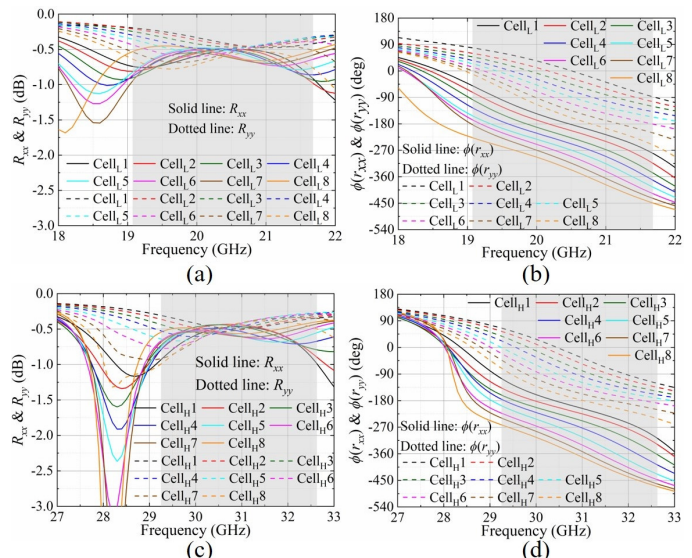


Fig. 5. Simulated LP scattering parameters at normal incidence of K -band (a) reflection magnitudes, (b) reflection phases, and Ka -band (c) reflection magnitudes, (d) reflection phases for the 8 cells of $Cell_L$ 1-8 and $Cell_H$ 1-8, respectively.

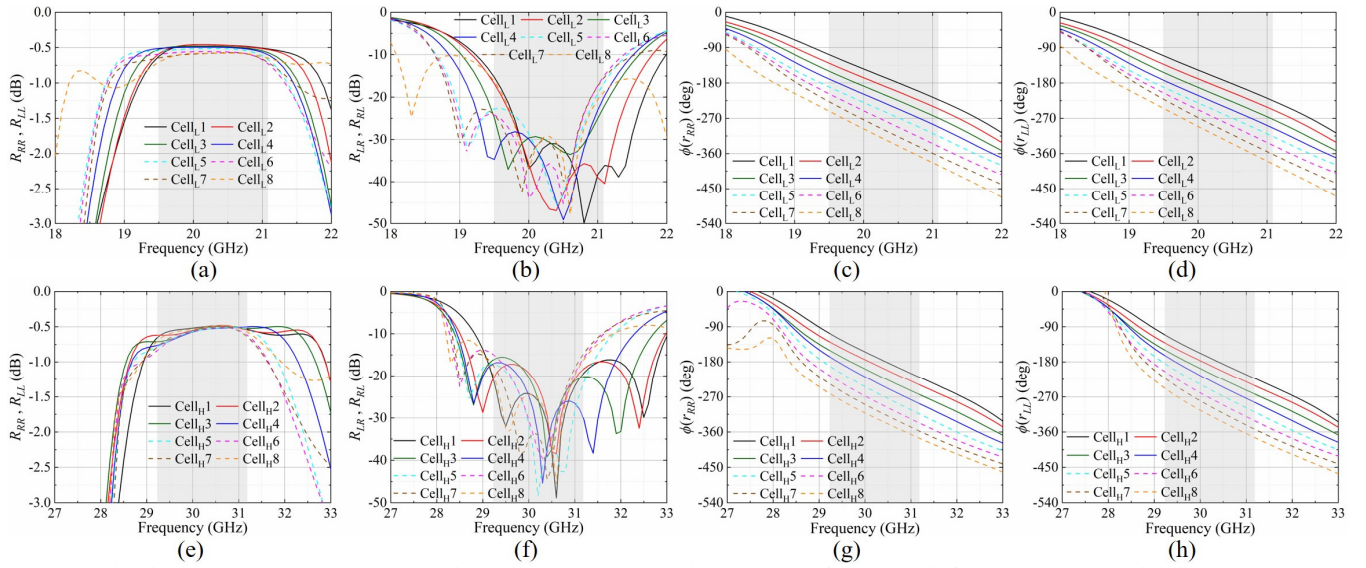


Fig. 6. Simulated CP scattering parameters at normal incidence of (a) R_{RR} , R_{LL} , (b) R_{RL} , R_{LR} , (c) $\phi(r_{RR})$, and (d) $\phi(r_{LL})$ at K -band. Simulated CP scattering parameters at normal incidence of (e) R_{RR} , R_{LL} , (f) R_{RL} , R_{LR} , (g) $\phi(r_{RR})$, and (h) $\phi(r_{LL})$ at Ka -band.

TABLE II 3×3 BIT DUAL-CP PHASE COMPENSATION STRATEGIES USING THE EIGHT CELLS WITH BP-DETERMINED ROTATION ANGLES.

$\phi(r_{LL})$ \ $\phi(r_{RR})$	0°	45°	90°	135°	180°	225°	270°	315°
0°	Cell _{LH11} * (C. _{LH5} , 135°)	Cell _{LH12} (C. _{LH4} , 123.75°)	Cell _{LH13} (C. _{LH3} , 112.5°)	Cell _{LH14} (C. _{LH2} , 101.25°)	Cell _{LH15} (C. _{LH1} , 90°)	Cell _{LH16} (C. _{LH8} , 168.75°)	Cell _{LH17} (C. _{LH7} , 157.5°)	Cell _{LH18} (C. _{LH6} , 146.25°)
45°	Cell _{LH21} (C. _{LH4} , 146.25°)	Cell _{LH22} (C. _{LH3} , 135°)	Cell _{LH23} (C. _{LH2} , 123.75°)	Cell _{LH24} (C. _{LH1} , 112.5°)	Cell _{LH25} (C. _{LH8} , 11.25°)	Cell _{LH26} (C. _{LH7} , 0°)	Cell _{LH27} (C. _{LH6} , 168.75°)	Cell _{LH28} (C. _{LH5} , 157.5°)
90°	Cell _{LH31} (C. _{LH3} , 157.5°)	Cell _{LH32} (C. _{LH2} , 146.25°)	Cell _{LH33} (C. _{LH1} , 135°)	Cell _{LH34} (C. _{LH8} , 33.75°)	Cell _{LH35} (C. _{LH7} , 22.5°)	Cell _{LH36} (C. _{LH6} , 11.25°)	Cell _{LH37} (C. _{LH5} , 0°)	Cell _{LH38} (C. _{LH4} , 168.75°)
135°	Cell _{LH41} (C. _{LH2} , 168.75°)	Cell _{LH42} (C. _{LH1} , 157.5°)	Cell _{LH43} (C. _{LH8} , 56.25°)	Cell _{LH44} (C. _{LH7} , 45°)	Cell _{LH45} (C. _{LH6} , 33.75°)	Cell _{LH46} (C. _{LH5} , 22.5°)	Cell _{LH47} (C. _{LH4} , 11.25°)	Cell _{LH48} (C. _{LH3} , 0°)
180°	Cell _{LH51} (C. _{LH1} , 0°)	Cell _{LH52} (C. _{LH8} , 78.75°)	Cell _{LH53} (C. _{LH7} , 67.5°)	Cell _{LH54} (C. _{LH6} , 56.25°)	Cell _{LH55} (C. _{LH5} , 45°)	Cell _{LH56} (C. _{LH4} , 33.75°)	Cell _{LH57} (C. _{LH3} , 22.5°)	Cell _{LH58} (C. _{LH2} , 11.25°)
225°	Cell _{LH61} (C. _{LH8} , 101.25°)	Cell _{LH62} (C. _{LH7} , 90°)	Cell _{LH63} (C. _{LH6} , 78.75°)	Cell _{LH64} (C. _{LH5} , 67.5°)	Cell _{LH65} (C. _{LH4} , 56.25°)	Cell _{LH66} (C. _{LH3} , 45°)	Cell _{LH67} (C. _{LH2} , 33.75°)	Cell _{LH68} (C. _{LH1} , 22.5°)
270°	Cell _{LH71} (C. _{LH7} , 112.5°)	Cell _{LH72} (C. _{LH6} , 101.25°)	Cell _{LH73} (C. _{LH5} , 90°)	Cell _{LH74} (C. _{LH4} , 78.75°)	Cell _{LH75} (C. _{LH3} , 67.5°)	Cell _{LH76} (C. _{LH2} , 56.25°)	Cell _{LH77} (C. _{LH1} , 45°)	Cell _{LH78} (C. _{LH8} , 123.75°)
315°	Cell _{LH81} (C. _{LH6} , 123.75°)	Cell _{LH82} (C. _{LH5} , 112.5°)	Cell _{LH83} (C. _{LH4} , 101.25°)	Cell _{LH84} (C. _{LH3} , 90°)	Cell _{LH85} (C. _{LH2} , 78.75°)	Cell _{LH86} (C. _{LH1} , 67.5°)	Cell _{LH87} (C. _{LH8} , 146.25°)	Cell _{LH88} (C. _{LH7} , 135°)

* The first row in the table is the cell number of the proposed 64 cells at K -band or Ka -band, while the first column of the second row donates the number of 8 cells, where C. is the abbreviation of Cell, and the second column represents the rotation angles, i.e., ϕ_r .

D. Interaction Between the K - and Ka -Band RA Cells

The K - and Ka -band cells can be rotated freely around the patch center in their own restricted circular areas with radii of R_{CL} and R_{CH} [see Fig. 2(b)], respectively. The gap between the restricted circles is G_C , where $R_{CL} + R_{CH} + G_C = 4.23$ mm. The value of G_C is set as 0.14 mm in this design by comprehensively considering fabrication accuracy and mutual coupling level between the K - and Ka -band phase delay lines. Importantly, the possible interaction between them during rotation needs to be investigated. This can be evaluated by observing the variation of CP reflection magnitudes and phases of the K -/ Ka -band cell while rotating the surrounding Ka -/ K -band cells. In Fig. 8(a), the scattering parameters are obtained when the K -band Cell_{L14} (and Cell_{L82}) are located in the center position with edge Ka -band Cell_{H1} (and Cell_{H5}) rotates from 0° to 157.5° at an interval of 22.5° . It can be seen from all the simulated results that the variation of the co-polarized CP reflection magnitudes is less than 0.1 dB at K -band, while the cross-polarized CP reflection magnitudes remain below -20 dB. Similarly, additional

simulations are carried out by considering the Ka -band Cell_{H66} (and Cell_{H45}) located in the center position with edge K -band Cell_{L1} (and Cell_{L5}) rotates from 0° to 157.5° at an interval of 22.5° . It can be seen that the co-polarized CP reflection magnitudes only have a minor fluctuation of less than 0.1 dB at Ka -band, while the cross-polarized CP reflection magnitudes are all below -20 dB [see Fig. 8(b)]. In addition, the co-polarized CP reflection phases at both K - and Ka -bands remain almost unchanged. Above all, it can be concluded that benefiting from the low mutual coupling, the influence on the K -/ Ka -band RA cell is negligible when rotating the surrounding Ka -/ K -band cells.

E. Performance of the RA Cells under Oblique Incidence

For a relatively large RA containing thousands of cells, the cells in the outer region are unavoidably illuminated by obliquely incident waves. Here, the oblique incidence response of the RA cells is studied. Cell_{L65} and Cell_{L77} are taken as examples at K -band, for an incident angle varying between 0° and 30° . The fluctuation of the co-polarized CP reflection

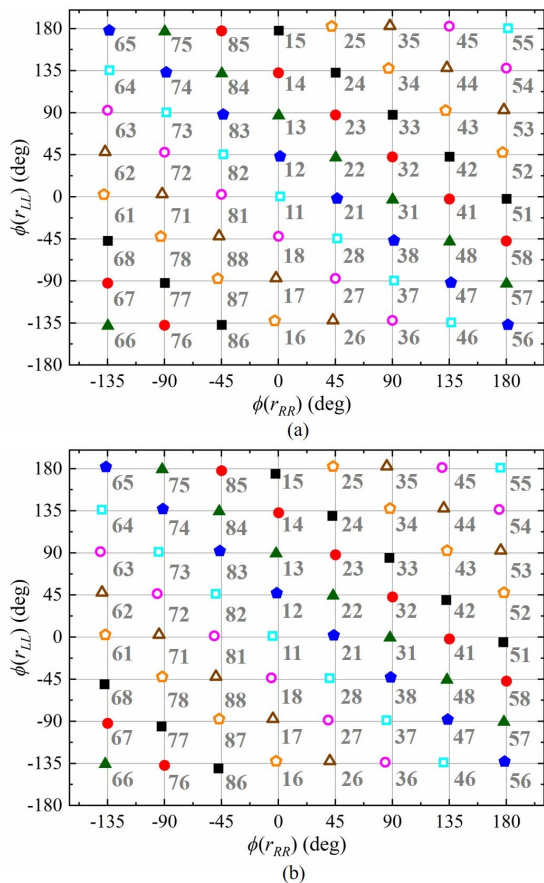


Fig. 7. Interstellar plots of the simulated co-polarized CP reflection phases ($\phi(r_{RR})$ and $\phi(r_{LL})$) for the 64 cells for 3×3 bit dual-CP phase shifting of LHCP/RHCP waves at (a) 20 and (b) 30 GHz.

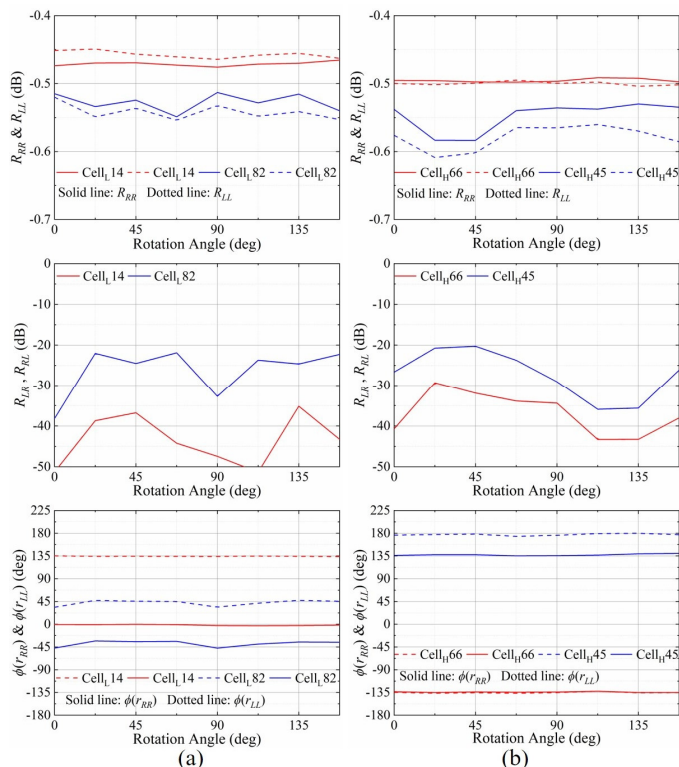


Fig. 8. Simulated CP reflection magnitudes (R_{RR} , R_{LL} , R_{LR} , R_{LR}) and co-polarized CP reflection phases ($\phi(r_{RR})$, $\phi(r_{LL})$) at normal incidence of (a) K -band RA cells (Cell₁₄, Cell₈₂) at 20 GHz surrounded by rotating Ka -band cell, and (b) Ka -band RA cells (Cell_{H66}, Cell_{H45}) at 30 GHz surrounded by rotating K -band cell.

magnitudes is less than 0.2 dB, while the cross-polarized CP reflection magnitudes are kept below -15 dB [see Fig. 9(a)]. Importantly, the co-polarized reflection phases remain almost unchanged. However, the angular stability becomes worse at Ka -band due to the relatively larger electrical element spacing. By taking Cell_{H64} and Cell_{H87} at Ka -band as examples, the co-polarized CP reflection magnitudes are above -1 dB, the cross-polarized CP reflection magnitudes are below -12 dB for incident angles of smaller than 15° [see Fig. 9(b)].

From this study, it can be concluded that the angular response at the higher frequency band would determine the proper range of the focus-to-diameter (F/D) ratio of the RA at Ka -band, where a relatively large F/D ratio is preferable.

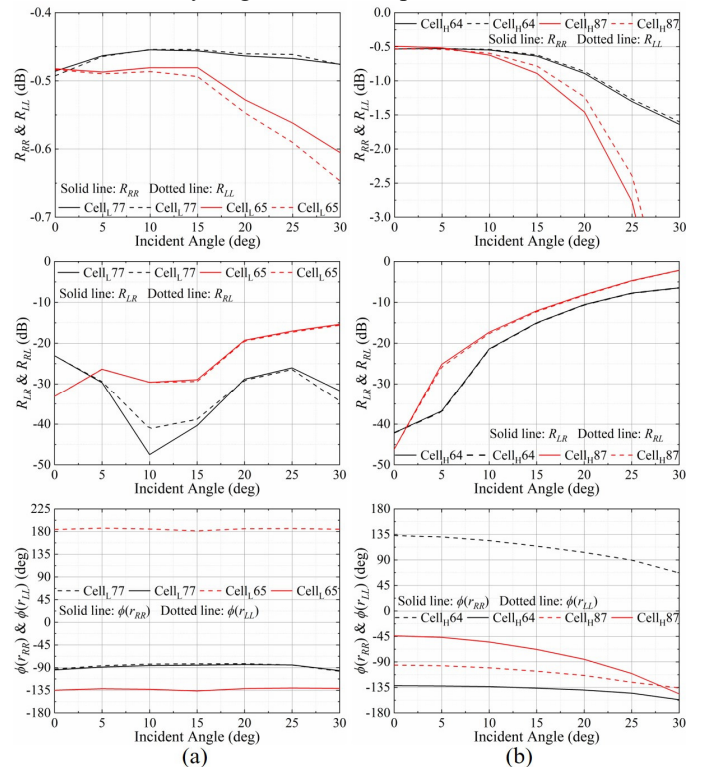


Fig. 9. Simulated CP reflection magnitudes (R_{RR} , R_{LL} , R_{LR} , R_{LR}) and co-polarized CP reflection phases ($\phi(r_{RR})$, $\phi(r_{LL})$) for selected RA cells as a function of incident angles of (a) Cell₇₇, Cell₆₅ at 20 GHz, and (b) Cell_{H64}, Cell_{H87} at 30 GHz.

III. DIFFRACTION ANALYSIS OF A SUPERCELL OF DUAL-WIDEBAND DUAL-CP RA CELLS

Before designing the finite-size RAs, the diffraction properties of an infinite periodic supercell containing a gradient array of the proposed dual-wideband dual-CP RA cells is investigated when it is illuminated by a plane wave. This can reveal the properties of the cells in a non-uniform environment and provide insight into the bandwidth and wave-bending behavior of the anomalous reflection functionality [41].

The supercell consists of eight K -band and eight Ka -band cells aligned along the y -axis with different phase gradients for RHCP and LHCP waves at each band [see Fig. 10(a)]. Specifically, the phase gradients of the supercell are $+45^\circ/90^\circ$ per cell for RHCP/LHCP waves at K -band and $0^\circ/45^\circ$ per cell for RHCP/LHCP waves at Ka -band [see Table III]. According

to the generalized law of reflection [42], the theoretically calculated deflection angles are $(\theta_{RR})_K = -18^\circ$, $(\theta_{LL})_K = 39^\circ$, $(\theta_{RR})_{Ka} = 0^\circ$, and $(\theta_{LL})_{Ka} = 12^\circ$ under a normally incident RHCP and LHCP plane wave at K - and Ka -bands, respectively. At 20 GHz, when excited by a RHCP/LHCP incident wave, the snapshots of the simulated distributions of the scattered E_x at $t = 0$ and E_y at $t = T/4$ are reported in Figs. 10(b) and (c). The scattered RHCP wave directs at $(\theta_{RR})_K = -18^\circ$, coupling into the -1^{st} -order diffraction mode, while the scattered LHCP wave couples into the $+2^{\text{nd}}$ -order diffraction mode with the beam tilting at $(\theta_{LL})_K = 39^\circ$. In addition, the simulated distributions of the scattered E_x at $t = 0$ and E_y at $t = T/4$ are presented in Figs. 10(d) and (e), when the supercell is illuminated by a RHCP/LHCP wave at 30 GHz. The RHCP wave reflects at $(\theta_{RR})_{Ka} = 0^\circ$ back to the 0^{th} -order diffraction mode, whereas the scattered LHCP wave directs at $(\theta_{LL})_{Ka} = 12^\circ$, coupling into the $+1^{\text{st}}$ -order diffraction mode.

TABLE III SELECTED CELLS AND PHASE GRADIENTS OF THE SUPERCELL FOR RHCP AND LHCP WAVES AT K - AND Ka -BANDS.

K-band	Cell _L Num.	Cell _L 11	Cell _L 27	Cell _L 35	Cell _L 43	Cell _L 51	Cell _L 67	Cell _L 75	Cell _L 83	Phase Gradient
	$\phi(r_{RR})$	0°	45°	90°	135°	180°	-135°	-90°	-45°	$\Delta\phi = +45^\circ$ $n = -1^{\text{st}}$
$\phi(r_{LL})$	0°	-90°	180°	90°	0°	-90°	180°	90°	$\Delta\phi = -90^\circ$ $n = +2^{\text{nd}}$	
Ka-band	Cell _H Num.	Cell _H 51	Cell _H 58	Cell _H 57	Cell _H 56	Cell _H 55	Cell _H 54	Cell _H 53	Cell _H 52	
	$\phi(r_{RR})$	180°	$\Delta\phi = 0^\circ$ $n = 0^{\text{th}}$							
$\phi(r_{LL})$	0°	-45°	-90°	-135°	180°	135°	90°	45°	$\Delta\phi = -45^\circ$ $n = +1^{\text{st}}$	

Moreover, the simulated scattering parameters as a function of frequency for different diffraction modes are present in Fig. 11. As can be seen from Fig. 11(a), when RHCP wave is incident on the supercell, the reflection magnitudes of R_{RR}^{-10} and R_{RR}^{00} are above -1 dB in the frequency ranges of 19.4 – 21.5 GHz and 29.5 – 31.7 GHz, respectively. Within the two bands, the power couples to the other unwanted diffraction modes are lower than -16.5 dB. In contrast, when a LHCP wave illuminates the supercell, in the bands spanning from 19.2 to 21.6 GHz at K -band and from 29.8 to 31.5 GHz at Ka -band, R_{LL}^{20} and R_{LL}^{10} are higher than -1 dB. Within the two bands, the reflection magnitudes of the other modes are below -14.6 dB.

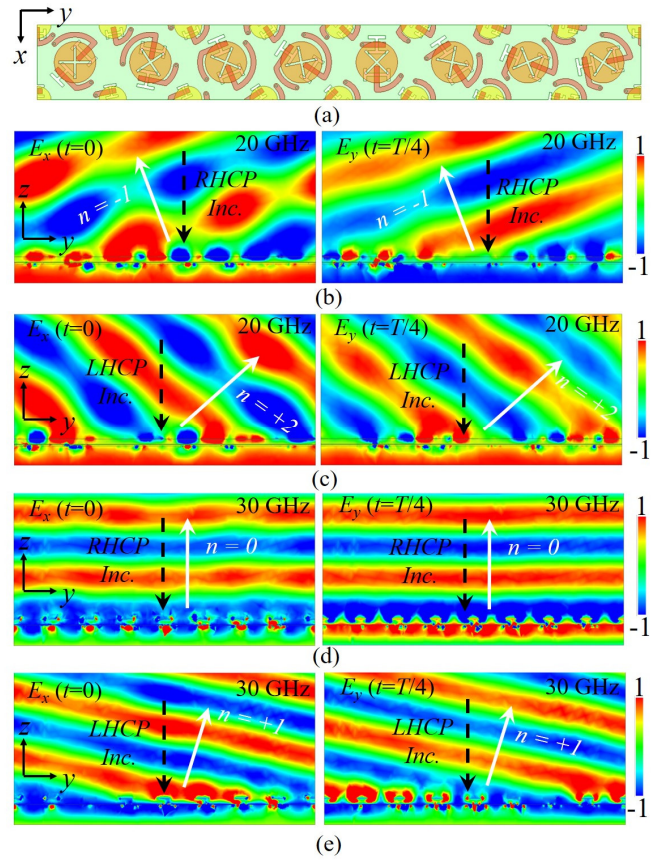


Fig. 10. (a) Configuration of the dual-wideband shared-aperture infinite periodic supercell. Snapshots of the simulated scattered electric fields (E_x at $t = 0$ and E_y at $t = T/4$) when the supercell is illuminated by a normally incident (b) RHCP wave at 20 GHz, (c) LHCP wave at 20 GHz, (d) RHCP wave at 30 GHz, and (e) LHCP wave at 30 GHz.

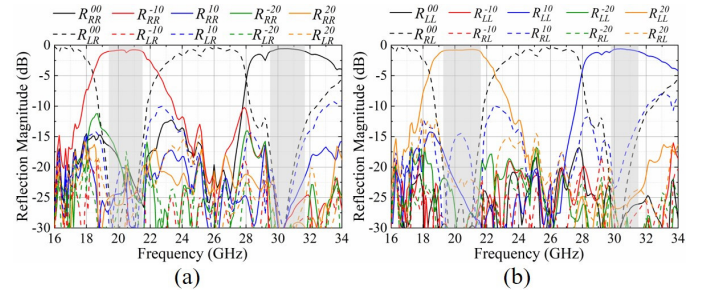


Fig. 11. Simulated CP reflection magnitudes of the dual-wideband shared-aperture infinite periodic supercell as a function of frequency for different diffraction modes when the incident wave is (a) RHCP and (b) LHCP.

IV. DESIGNS AND EXPERIMENTAL VERIFICATIONS OF TWO DUAL-WIDEBAND DUAL-CP RAS

Based on the proposed RA cells, two proof-of-concept dual-wideband dual-CP RAs with different beam directions are designed, fabricated, and experimentally characterized. Both RAs have a diameter of 180 mm, consisting of 1381 cells, i.e., 716 K -band cells and 665 Ka -band cells. Two K -band and two Ka -band conical CP horns with different handedness are utilized as the feeds. The K -band CP horn has a gain of 16 dBic with a -10 dB beamwidth of 50.8° , while the Ka -band CP horn offers a gain of 21 dBic and a -10 dB beamwidth of 28° . By limiting the oblique incident angle for the edge cells to be no

more than 23° and 21° , the focal distances between the horn and RA are set as F_K (216 mm) and F_{Ka} (226.2 mm) at K - and Ka -bands, respectively, corresponding to an F_K/D ratio of 1.2 and an F_{Ka}/D ratio of 1.3.

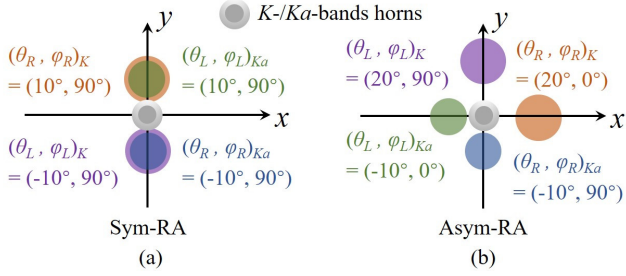


Fig. 12. Illustration of the horn location and directions of the four generated beams for the (a) Sym-RA and (b) Asym-RA.

A. Dual-Wideband Dual-CP RA Designs

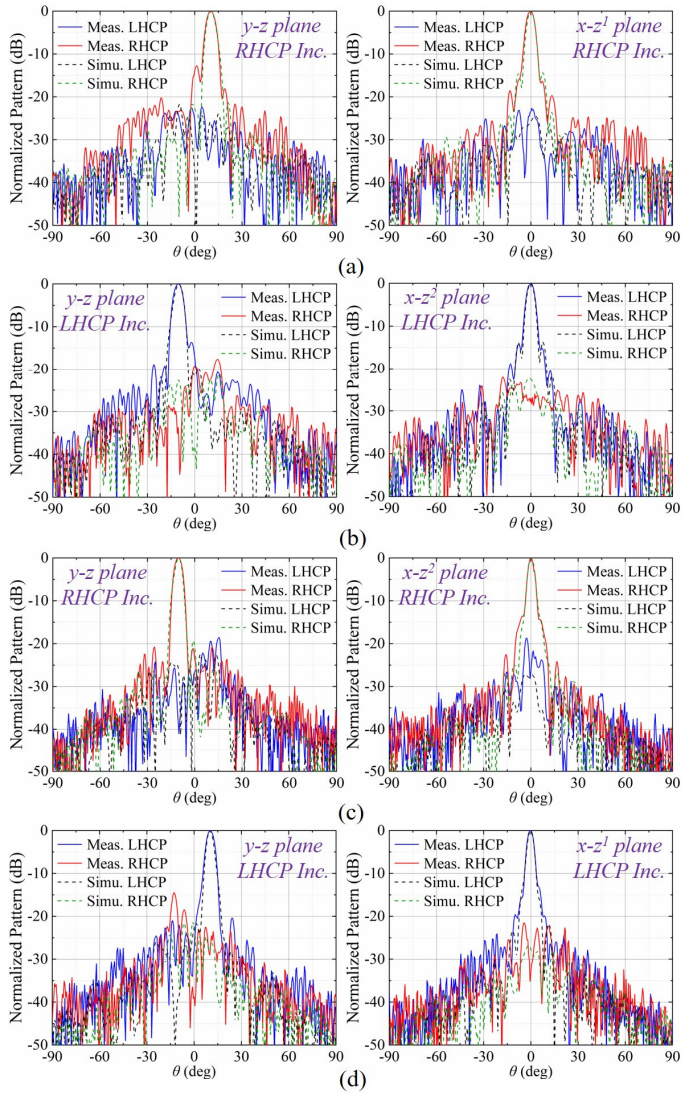


Fig. 13. Simulated and measured normalized radiation patterns in the two orthogonal planes cutting through the main beam of the Sym-RA (a) at 20 GHz with RHCP feed, (b) at 20 GHz with LHCP feed, (c) at 30 GHz with RHCP feed, and (d) at 30 GHz with LHCP feed, where $\hat{z}^1 = \hat{z}\cos 10^\circ + \hat{y}\sin 10^\circ$ and $\hat{z}^2 = \hat{z}\cos 10^\circ - \hat{y}\sin 10^\circ$.

The proposed K - and Ka -band cells with 3-bit dual-CP precision are utilized for transforming the spherical wavefront

of the radiated wave from the feed horns into highly-directive pencil beams [4], [43]. The feed horns together with the finite-sized RA are simulated in HFSS using the hybrid finite element-boundary integral (FE-BI) method [35]. Two RAs with different beam directions are designed for verifying the dual-wideband dual-CP performance.

The first RA has orthogonal CP beams symmetrically distributed in the y - z plane for both K - and Ka -bands, which is referred to as Sym-RA. It generates four beams, which are K -band RHCP and Ka -band LHCP beams pointing at $(10^\circ, 90^\circ)$, as well as K -band LHCP and Ka -band RHCP beams directing at $(-10^\circ, 90^\circ)$ [see Fig. 12(a)]. The simulated normalized CP radiation patterns in the y - z plane and x - z^1 plane (or x - z^2 plane) of the four beams generated by the Sym-RA are provided in Fig. 13. The beam directions are consistent with the designed ones. The simulated sidelobe levels (SLLs) and cross-polarization levels are $-14.2/-13.7$ dB and $-25.8/-22.5$ dB for the K -band RHCP/LHCP beams, respectively [see Figs. 13(a) - (b)]. The simulated bandwidths are 13.4% and 15.1% for the K -band RHCP and LHCP beams with both the gain variation and AR smaller than 2 dB, respectively, as shown in Figs. 14(a) - (b). The simulated peak gains are 27.3 and 27.4 dBic for RHCP and LHCP waves at K -band, corresponding to aperture efficiencies of 37.8% and 38.3%. At Ka -band, the simulated SLLs and cross-polarization levels are $-19.3/-21.5$ dB and $-27.5/-27.7$ dB for RHCP and LHCP beams, respectively [see Figs. 13(c) - (d)]. The produced RHCP beam owns a simulated bandwidth of 10.4% with both the gain variation and AR smaller than 2 dB, whereas such bandwidth is about 8% for the LHCP beam, as presented in Figs. 14(c) - (d). The simulated peak gains for the Ka -band RHCP and LHCP beams are 29.9 and 30.1 dBic, indicating aperture efficiencies of 32.9% and 34.4%, respectively.

The second RA produces four asymmetrically distributed pencil beams, which is named as Asym-RA. The four generated beams are K -band RHCP/LHCP beams pointing at $(20^\circ, 0^\circ)/(20^\circ, 90^\circ)$, and Ka -band RHCP/LHCP beams directing at $(-10^\circ, 90^\circ)/(-10^\circ, 0^\circ)$ [see Fig. 12(b)]. The simulated normalized radiation patterns in the two orthogonal planes cutting through the four main beams are shown in Fig. 15, the beams point to the desirable directions as the design intended. The simulated SLLs and cross-polarization levels are $-16.2/-17.7$ dB and $-29.7/-31.7$ dB for RHCP/LHCP wave at K -band as shown in Figs. 15(a) and (b). The simulated bandwidths are 13.9% and 14.9% for K -band RHCP and LHCP beams with both the gain variation and AR smaller than 2 dB [see Figs. 16(a) and (b)]. The simulated peak gains for K -band RHCP and LHCP waves are 27.3 and 27.4 dBic, corresponding to aperture efficiencies of 38.1% and 38.9%. When the Ka -band horns are employed as feeds, the simulated SLLs and cross-polarization levels are $-21.8/-19.1$ dB and $-26.7/-28.3$ dB for the RHCP/LHCP waves as shown in Figs. 15(c) and (d). The Ka -band RHCP and LHCP beams achieve simulated bandwidths of 11.3% and 11.7% with both the gain variation and AR smaller than 2 dB [see Fig. 16(c) and (d)]. The simulated peak gains reach 30.2 and 30.3 dBic, indicating aperture efficiency values of 34.7% and 35.9%, for Ka -band RHCP and LHCP waves.

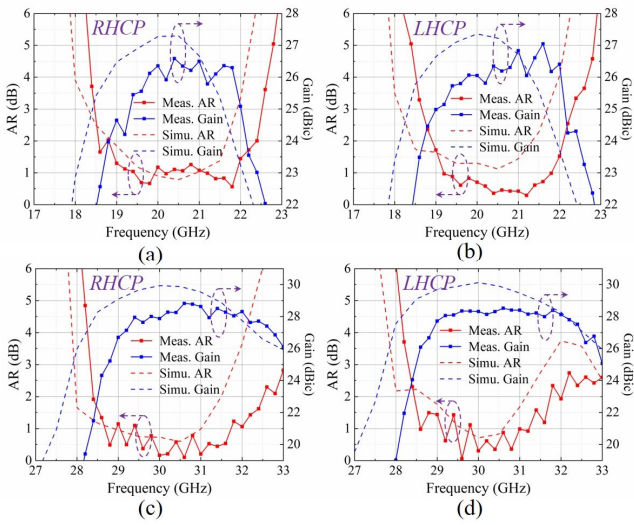


Fig. 14. Simulated and measured peak gain and AR as a function of frequency for the Sym-RA excited by the (a) *K*-band RHCP, (b) *K*-band LHCP, (c) *Ka*-band RHCP, and (d) *Ka*-band LHCP feed horn, respectively.

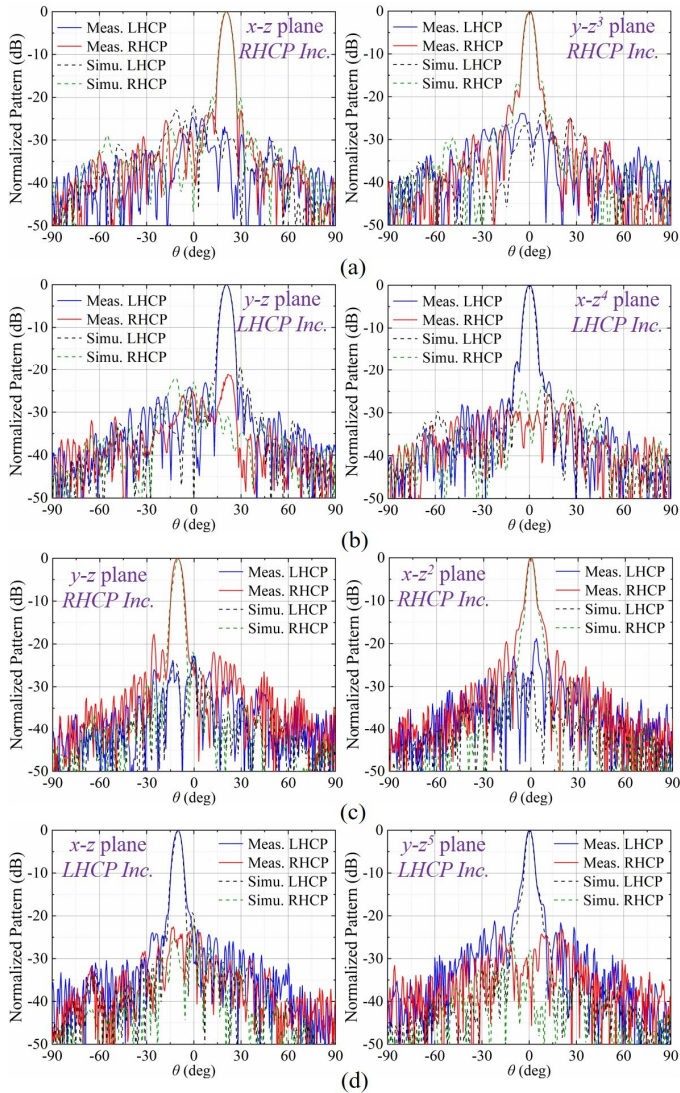


Fig. 15. Simulated and measured normalized radiation patterns in the two orthogonal planes cutting through the main beam of the Asym-RA (a) at 20 GHz with RHCP feed, (b) at 20 GHz with LHCP feed, (c) at 30 GHz with RHCP feed, and (d) at 30 GHz with LHCP feed, where $\hat{z}^3 = \hat{z}\cos 20^\circ + \hat{x}\sin 20^\circ$, $\hat{z}^4 = \hat{z}\cos 20^\circ + \hat{y}\sin 20^\circ$, and $\hat{z}^5 = \hat{z}\cos 10^\circ - \hat{x}\sin 10^\circ$.

B. Experiments

Both the Sym-RA and Asym-RA were fabricated and measured in a far-field anechoic chamber. The photograph of the RA is provided in Fig. 17(a), where the insert shows an enlarged view of a portion of the shared-aperture RA cells. The measurement environment in the far-field chamber is provided in Fig. 17(b). When the scanning plane cutting through the main beam lies in the *x-z* or *y-z* plane, the patterns can be measured directly by placing the RA on the turntable. For the other orthogonal plane not coinciding with the *x-z* or *y-z* plane, a glass wedge with an angle of 10° or 20° was inserted underneath the frame for tilting the beam towards the horn.

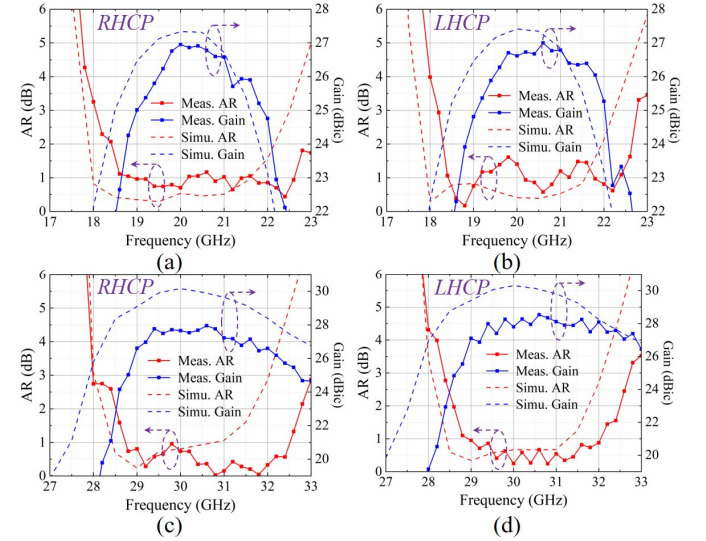


Fig. 16. Simulated and measured peak gain and AR as a function of frequency for the Asym-RA excited by the (a) *K*-band RHCP, (b) *K*-band LHCP, (c) *Ka*-band RHCP, and (d) *Ka*-band LHCP feed horn, respectively.

The measured normalized CP radiation patterns in the *y-z* plane and *x-z*¹ plane (or *x-z*² plane) of the Sym-RA are presented in Fig. 13, which agree well with the simulated results. The measured SLLs and cross-polarization levels for the *K*-band RHCP/LHCP beams are $-12.7/-13.6$ dB and $-23.4/-27$ dB [see Figs. 13(a) - (b)]. The measured bandwidths are 14.4% and 14.6% with both the gain variation and AR smaller than 2 dB, i.e., in the frequency range of 19.3 – 22.3 GHz, and 19.1 – 22.1 GHz for RHCP and LHCP beams at *K*-band as shown in Figs. 14(a) and (b). The measured peak gains are 26.6 and 27 dBic for RHCP and LHCP waves at *K*-band, corresponding to measured aperture efficiencies of 32.1% and 35.7%. With *Ka*-band feed horns, the measured SLLs and cross-polarization levels are $-21.1/-19.9$ dB and $-26.4/-29.1$ dB for the RHCP/LHCP beams, respectively [see Figs. 13(c) - (d)]. At *Ka*-band, the produced RHCP beam owns a measured bandwidth of 11.4% (29 – 32.5 GHz) with both the gain variation and AR smaller than 2 dB, whereas such bandwidth is 9.6% (28.8 – 31.7 GHz) for the LHCP beam as presented in Figs. 14(c) - (d). The measured peak gains and aperture efficiencies are 28.8/28.5 dBic and 25.6%/23.8% for RHCP/LHCP beams at *Ka*-band.

REFERENCE

- [1] S. Gao, Q. Luo, and F. Zhu, *Circularly Polarized Antennas*. Hoboken, NJ, USA: Wiley, 2013.
- [2] Y. Hu, J. Zhan, Z. H. Jiang, C. Yu, and W. Hong, "An orthogonal hybrid analog-digital multibeam antenna array for millimeter-wave massive MIMO systems," *IEEE Trans. Antennas Propag.*, vol. 69, no. 3, pp. 1393-1403, Mar. 2021.
- [3] S. K. Rao, "Parametric design and analysis of multiple-beam reflector antennas for satellite communications," *IEEE Antennas Propag. Mag.*, vol. 45, no. 4, pp. 26-34, Aug. 2003.
- [4] J. Huang and J. A. Encinar, *Reflectarray Antennas*. New York, NY, USA: Wiley, 2008.
- [5] G. Zhao, Y. Jiao, F. Zhang, and F. Zhang, "A subwavelength element for broadband circularly polarized reflectarrays," *IEEE Antennas Wireless Propag. Lett.*, vol. 9, pp. 330-333, 2010.
- [6] E. Carrasco, M. Barba, and J. A. Encinar, "Reflectarray element based on aperture-coupled patches with slots and lines of variable length," *IEEE Trans. Antennas Propag.*, vol. 55, no. 3, pp. 820-825, Mar. 2007.
- [7] J. A. Encinar, and J. A. Zornoza, "Three-layer printed reflectarrays for contoured beam space applications," *IEEE Trans. Antennas Propag.*, vol. 52, no. 5, pp. 1138-1148, May 2004.
- [8] X. Xia, Q. Wu, H. Wang, C. Yu, and W. Hong, "Wideband millimeter-wave microstrip reflectarray using dual-resonance unit cells," *IEEE Antennas Wireless Propag. Lett.*, vol. 16, pp. 4-7, 2017.
- [9] H. Hasani, C. Peixeiro, A. K. Skrivervik, and J. Perruisseau-Carrier, "Single-layer quad-band printed reflectarray antenna with dual linear polarization," *IEEE Trans. Antennas Propag.*, vol. 63, no. 12, pp. 5522-5528, Dec. 2015.
- [10] R. Deng, S. Xu, F. Yang, and M. Li, "An FSS-backed Ku/Ka quad-band reflectarray antenna for satellite communications," *IEEE Trans. Antennas Propag.*, vol. 66, no. 8, pp. 4353-4358, Aug. 2018.
- [11] Dau-Chyrh Chang, and Ming-Chih Huang, "Multiple-polarization microstrip reflectarray antenna with high efficiency and low cross-polarization," *IEEE Trans. Antennas Propag.*, vol. 43, no. 8, pp. 829-834, Aug. 1995.
- [12] X. Zhang, F. Yang, S. Xu, A. Aziz, and M. Li, "Hybrid polarization-phase tuning methodology for reflectarray antennas," *IEEE Trans. Antennas Propag.*, vol. 69, no. 9, pp. 5534-5545, Sep. 2021.
- [13] P. Nayeri, F. Yang, and A. Z. Elsherbeni, "Beam-scanning reflectarray antennas: a technical overview and state of the art," *IEEE Antennas Propag. Mag.*, vol. 57, no. 4, pp. 32-47, Aug. 2015.
- [14] J. Yang, Y. Shen, L. Wang, H. Meng, W. Dou, and S. Hu, "2-D scannable 40-GHz folded reflectarray fed by SIW slot antenna in single-layered PCB," *IEEE Trans. Microw. Theory Techn.*, vol. 66, no. 6, pp. 3129-3135, Jun. 2018.
- [15] Y. Hu, W. Hong, and Z. H. Jiang, "A multibeam folded reflectarray antenna with wide coverage and integrated primary sources for millimeter-wave massive MIMO applications," *IEEE Trans. Antennas Propag.*, vol. 66, no. 12, pp. 6875-6882, Dec. 2018.
- [16] Y. Mao, S. Xu, F. Yang, and A. Z. Elsherbeni, "A novel phase synthesis approach for wideband reflectarray design," *IEEE Trans. Antennas Propag.*, vol. 63, no. 9, pp. 4189-4193, Sep. 2015.
- [17] R. Deng, S. Xu, F. Yang, and M. Li, "Single-layer dual-band reflectarray antennas with wide frequency ratios and high aperture efficiencies using phoenix elements," *IEEE Trans. Antennas Propag.*, vol. 65, no. 2, pp. 612-622, Feb. 2017.
- [18] R. Chaharmir, J. Shaker, and M. Cuhaci, "Development of dual-band circularly polarised reflectarray," *Inst. Elect. Eng. Proc., Microw. Antennas Propag.*, vol. 153, no. 1, pp. 49-54, Feb. 2003.
- [19] E. Martinez-de-Rioja, J. A. Encinar, M. Barba, R. Florencio, R. R. Boix, and V. Losada, "Dual polarized reflectarray transmit antenna for operation in Ku- and Ka-bands with independent feeds," *IEEE Trans. Antennas Propag.*, vol. 65, no. 6, pp. 3241-3246, Jun. 2017.
- [20] Y. Chen, L. Chen, H. Wang, X. Gu, and X. Shi, "Dual-band crossed-dipole reflectarray with dual-band frequency selective surface," *IEEE Antennas Wireless Propag. Lett.*, vol. 12, pp. 1157-1160, 2013.
- [21] T. Smith, U. Gothelf, O. S. Kim, and O. Breinbjerg, "Design, manufacturing, and testing of a 20/30-GHz dual-band circularly polarized reflectarray antenna," *IEEE Antennas Wireless Propag. Lett.*, vol. 12, pp. 1480-1483, 2013.
- [22] R. Deng, Y. Mao, S. Xu, and F. Yang, "A single-layer dual-band circularly polarized reflectarray with high aperture efficiency," *IEEE Trans. Antennas Propag.*, vol. 63, no. 7, pp. 3317-3320, Jul. 2015.
- [23] T. Smith, U. Gothelf, O. S. Kim, and O. Breinbjerg, "An FSS-backed 20/30 GHz circularly polarized reflectarray for a shared aperture L- and Ka-band satellite communication antenna," *IEEE Trans. Antennas Propag.*, vol. 62, no. 2, pp. 661-668, Feb. 2014.
- [24] C. Han, J. Huang, and Kai Chang, "A high efficiency offset-fed X/ka-dual-band reflectarray using thin membranes," *IEEE Trans. Antennas Propag.*, vol. 53, no. 9, pp. 2792-2798, Sep. 2005.
- [25] M. R. Chaharmir, and J. Shaker, "Design of a multilayer X-/Ka-band frequency-selective surface-backed reflectarray for satellite applications," *IEEE Trans. Antennas Propag.*, vol. 63, no. 4, pp. 1255-1262, Apr. 2015.
- [26] Z. H. Jiang, Y. Zhang, and W. Hong, "Anisotropic impedance surface-enabled low-profile broadband dual-circularly polarized multibeam reflectarrays for Ka-band applications," *IEEE Trans. Antennas Propag.*, vol. 68, no. 8, pp. 6441-6446, Aug. 2020.
- [27] S. Mener, R. Gillard, R. Sauleau, C. Cheymol, and P. Potier, "Design and characterization of a CPSS-based unit-cell for circularly polarized reflectarray applications," *IEEE Trans. Antennas Propag.*, vol. 61, no. 4, pp. 2313-2318, Apr. 2013.
- [28] S. Mener, R. Gillard, R. Sauleau, A. Bellion, and P. Potier, "Dual circularly polarized reflectarray with independent control of polarizations," *IEEE Trans. Antennas Propag.*, vol. 63, no. 4, pp. 1877-1881, Apr. 2015.
- [29] C. S. Geaney, M. Hosseini, and S. V. Hum, "Reflectarray antennas for independent dual linear and circular polarization control," *IEEE Trans. Antennas Propag.*, vol. 67, no. 9, pp. 5908-5918, Sep. 2019.
- [30] M. Joyal, R. El Hani, M. Riel, Y. Demers, and J. Laurin, "A reflectarray-based dual-surface reflector working in circular polarization," *IEEE Trans. Antennas Propag.*, vol. 63, no. 4, pp. 1306-1313, Apr. 2015.
- [31] Z. H. Jiang, T. Yue, and W. Hong, "Low-profile and wideband dual-circularly polarized reflect-arrays based on rotated metal-backed dual-polarized aperture-coupled patch elements," *IEEE Trans. Antennas Propag.*, vol. 68, no. 3, pp. 2108-2117, Mar. 2020.
- [32] R. Florencio, J. A. Encinar, R. R. Boix, M. Barba, and G. Toso, "Flat reflectarray that generates adjacent beams by discriminating in dual circular polarization," *IEEE Trans. Antennas Propag.*, vol. 67, no. 6, pp. 3733-3742, Jun. 2019.
- [33] W. Guo, G. Wang, W. Ji, Y. Zheng, K. Chen, and Y. Feng, "Broadband spin-decoupled metasurface for dual-circularly polarized reflector antenna design," *IEEE Trans. Antennas Propag.*, vol. 68, no. 5, pp. 3534-3543, May 2020.
- [34] Q. Luo *et al.*, "Multibeam dual-circularly polarized reflectarray for connected and autonomous vehicles," *IEEE Trans. Veh. Technol.*, vol. 68, no. 4, pp. 3574-3585, Apr. 2019.
- [35] P. Naseri, M. Riel, Y. Demers, and S. V. Hum, "A dual-band dual-circularly polarized reflectarray for K/Ka-band space applications," *IEEE Trans. Antennas Propag.*, vol. 68, no. 6, pp. 4627-4637, Jun. 2020.
- [36] P. Naseri, S. A. Matos, J. R. Costa, C. A. Fernandes, and N. J. G. Fonseca, "Dual-band dual-linear-to-circular polarization converter in transmission mode application to K/Ka-band satellite communications," *IEEE Trans. Antennas Propag.*, vol. 66, no. 12, pp. 7128-7137, Dec. 2018.
- [37] P. Xu, L. Li, R. Li, and H. Liu, "Dual-circularly polarized spin-decoupled reflectarray with FSS-back for independent operating at Ku/Ka-band," *IEEE Trans. Antennas Propag.*, vol. 69, no. 10, pp. 7041-7046, Oct. 2021.
- [38] C. Wang, and L. Chen, "Modeling of stepped-impedance slot antenna," *IEEE Trans. Antennas Propag.*, vol. 62, no. 2, pp. 955-959, Feb. 2014.
- [39] Y. Yoshimura, "A microstripline slot antenna," *IEEE Trans. Microw. Theory Techn.*, vol. 20, no. 11, pp. 760-762, Nov. 1972.
- [40] J. Huang, and R. J. Pogorzelski, "A Ka-band microstrip reflectarray with elements having variable rotation angles," *IEEE Trans. Antennas Propag.*, vol. 46, no. 5, pp. 650-656, May 1998.
- [41] Z. H. Jiang, L. Kang, W. Hong, and D. H. Werner, "Highly efficient broadband multiplexed millimeter-wave vortices from metasurface-enabled transmit-arrays of subwavelength thickness," *Phys. Rev. Appl.*, vol. 9, no. 6, Jun. 2018, Art. no. 064009.
- [42] N. Yu, P. Genevet, M. A. Kats, F. Aieta, J.-P. Tetienne, F. Capasso, and Z. Gaburro, "Light propagation with phase discontinuities: generalized laws of reflection and refraction," *Science*, vol. 334, no. 6054, pp. 333-337, Oct. 2011.
- [43] Z. H. Jiang, L. Kang, T. Yue, W. Hong, and D. H. Werner, "Wideband transmit arrays based on anisotropic impedance surfaces for circularly polarized single-feed multibeam generation in the Q-band," *IEEE Trans. Antennas Propag.*, vol. 68, no. 1, pp. 217-229, Jan. 2020.



Xuanfeng Tong (S'20) was born in Taizhou, Jiangsu, China, in 1993. He received the B.S. degree from Chifeng University, Chifeng, China, in 2016, and the M.S. degree from the School of Electronic Information, Soochow University, Suzhou, China, in 2019. He is currently pursuing the Ph.D degree with

Southeast University, Nanjing, China.

His main research interests include dual-band and dual-polarized antenna, reflectarray and transmitarray.

Mr. Tong was a recipient of the 2018 Nation Scholarship for Graduate Students and the Best Student Paper Award at the 2021 IEEE International Workshop on Electromagnetics (iWEM), Guangzhou, China.



Zhi Hao Jiang (S'07–M'13) was born in Nanjing, China, in 1986. He received the B.S. degree in radio engineering from Southeast University, Nanjing, in 2008, and the Ph.D. degree in electrical engineering from The Pennsylvania State University, University Park, State College, PA, USA, in 2013. From 2013 to 2016, he was a Post-

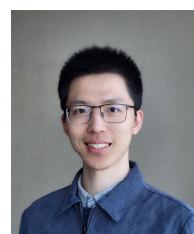
Doctoral Fellow with the Computational Electromagnetics and Antennas Research Laboratory, Department of Electrical Engineering, The Pennsylvania State University. He is currently a Professor with the State Key Laboratory of Millimeter Waves, School of Information Science and Engineering, Southeast University.

Dr. Jiang has authored or co-authored more than 100 papers in peer-reviewed journals, over 70 papers in conference proceedings, as well as 9 book chapters. He has also co-edited two books: *Electromagnetic Vortices: Wave Phenomena and Engineering Applications* (Wiley/IEEE Press, 2021), *Electromagnetics of Body-Area Networks: Antennas, Propagation, and RF Systems* (Wiley/IEEE Press, 2016). He holds 7 granted U.S. patents and 15 granted Chinese patents. He has served as the TPC Co-Chair or a TPC Member for multiple international conferences. He was a recipient of the Outstanding Youth Scholar of National Science Foundation of China in 2021, the IEEE Microwave Prize in 2021, the Young Scientist Award at the URSI-GASS in 2020, the Young Scientist Award at the 2019 ACES-China Conference, the High-Level Innovative and Entrepreneurial Talent presented by Jiangsu Province, China, in 2017, the Thousands of Young Talents presented by China government in 2016, the 2012 A. J. Ferraro Outstanding Doctoral Research Award in Electromagnetics, and several best (student) paper awards at international conferences. He is a Senior Member of CIE, serves as the Associate Editor of *IET Communications*, was a Guest Editor of *International Journal of RF and Microwave Computer-Aided Engineering*. His current research interests include microwave/millimeter-wave antennas and circuits, millimeter-wave systems, impedance surfaces, metamaterials, and analytical methods.



Yuan Li (S'21) was born in Huainan, Anhui, China, in 1994. He received the B.S. degree from University of Electronic Science and Technology of China (UESTC), Chengdu, China, in 2017. He is currently pursuing the Ph.D degree with Southeast University, Nanjing, China.

His main research interests include circular polarization selective surface, metasurface, reflectarray and transmitarray.



Fan Wu (S'15–M'18) was born in Jiangxi, China. He received the B.Eng and M.Eng degrees in electronic engineering from Beijing Jiaotong University, Beijing, China, in 2012 and 2015, respectively, and the Ph.D. degree in electronic engineering from City University of Hong Kong, Hong Kong, in 2018.

He is currently an Assistant Professor with the State Key Laboratory of Millimeter Waves, School of Information Science and Engineering, Southeast University, Nanjing, China. His current research is in the areas of space-fed antennas, circularly-polarized wideband antennas and reconfigurable antenna designs.

Dr. Wu was a recipient of the Honorable Mention at the student contest of the 2018 IEEE APS-URSI Conference and Exhibition held in Boston, USA. He served as a regular reviewer for numerous peer-reviewed international journals including the IEEE T-AP and AWPL.



Ronan Sauleau (M'04–SM'06–F'18) graduated in electrical engineering and radio communications from the Institut National des Sciences Appliquées, Rennes, France, in 1995. He received the Agrégation degree from the Ecole Normale Supérieure de Cachan, France, in 1996, and the

Doctoral degree in signal processing and telecommunications and the “Habilitation à Diriger des Recherches” degree, both from the University of Rennes 1, France, in 1999 and 2005, respectively. He was an Assistant Professor and Associate Professor at the University of Rennes 1, between September 2000 and November 2005, and between December 2005 and October 2009, respectively. He has been appointed as a full Professor in the same University since November 2009.

His current research fields are numerical modeling, millimeter-wave beam steering antennas, substrate integrated waveguide antennas, lens-based focusing devices, periodic and non-periodic structures (FSS, metasurfaces, polarizers, reflectarrays, and transmitarrays) and biological effects of millimeter waves.

He has been involved in more than 70 research projects at the national and European levels and has co-supervised 27 post-doctoral fellows, 57 PhD students and 50 master students.

He has received 20 patents and is the author or coauthor of more than 275 journal papers and 570 publications in international conferences and workshops. He was co-director of the research Department ‘Antenna and Microwave Devices’ at IETR and deputy director of IETR between 2012 and 2016. He is now director of IETR. Prof. Sauleau received the 2004 ISAP Conference Young Researcher Scientist Fellowship (Japan) and the first Young Researcher Prize in Brittany, France, in 2001 for his research work on gain-enhanced Fabry-Perot antennas. In September 2007, he was elevated to Junior member of the “Institut Universitaire de France”. He was awarded the Bronze medal by CNRS in 2008, and the silver medal in 2020. He received the 2021 Antenna EurAAP Award. He was the co-recipient of several international conference awards with some of his students (Int. Sch. of BioEM 2005, BEMS'2006, MRRS'2008, E-MRS'2011, BEMS'2011, IMS'2012, Antem'2012, BioEM'2015, EuCAP'2019, EuCAP'2021). He served as a guest editor for the IEEE Antennas Propagat. Special Issue on “Antennas and Propagation at mm and sub mm waves”. He served as a national delegate for several EU COST actions. He has served as a national delegate for EurAAP and as a member of the board of Director of EurAAP from 2013 to 2018.



Wei Hong (M'92–SM'07–F'12) received the B.S. degree from the University of Information Engineering, Zhengzhou, China, in 1982, and the M.S. and Ph.D. degrees from Southeast University, Nanjing, China, in 1985 and 1988, respectively, all in radio engineering.

He has been with the State Key Laboratory of Millimeter Waves, Southeast University, since 1988, where he has also been the Director of the Laboratory since 2003. He is currently a Professor of the School of Information Science and Engineering with Southeast University. In 1993 and 1995–1998, he was a short-term Visiting Scholar with the University of California at Berkeley and at Santa Cruz, CA, USA, respectively. He has authored or co-authored over 300 technical publications and authored two books. His current research interests include numerical methods for electromagnetic problems, millimeter-wave theory and technology, antennas, electromagnetic scattering, and RF technology for mobile communications

Dr. Hong was an Elected IEEE MTT-S AdCom Member during 2014–2016. He is a fellow of IEEE and CIE. He twice awarded the National Natural Prizes, and thrice awarded the first-class Science and Technology Progress Prizes issued by the Ministry of Education of China and Jiangsu Province Government. Besides, he also received the Foundations for China Distinguished Young Investigators and for “Innovation Group” issued by the NSF of China. He is the Vice President of the CIE Microwave Society and Antenna Society and the Chair of the IEEE MTTs/APS/EMCS Joint Nanjing Chapter. He served as the Associate Editor of the IEEE TRANSACTIONS ON MICROWAVE THEORY AND TECHNIQUES from 2007 to 2010, and one of the Guest Editors for the 5G special issue of the IEEE TRANSACTIONS ON ANTENNAS AND PROPAGATION in 2017.